JMEPEG (2023) 32:3853–3870
https://doi.org/10.1007/s11665-023-08206-8

1059-9495/$19.00

TECHNICAL ARTICLE

On the Use of a Hybrid Metallic-Composite Design to Increase Mechanical Performance of an Automotive Chassis

A. Garofano, V. Acanfora, F. Fittipaldi, and A. Riccio

Submitted: 7 October 2022 / Revised: 23 March 2023 / Accepted: 2 April 2023 / Published online: 24 April 2023

Thanks to the introduction of high-performance composite materials, 'metal replacement' approaches are successfully gaining ground even in the most challenging engineering applications. Among these, one of the most recent application challenges is improving the driving range of Battery Electric Vehicles (BEVs) by adopting innovative materials to lighten the mass of structural components, thus reducing energy requirements and enabling the use of smaller and less expensive batteries. Hence, in the present work, the employment of laminated composite panels in an electric minibus chassis is investigated as an effective way to reduce the global mass of the chassis' structure and, at the same time, to increase its structural performances in terms of torsional stiffness and crashworthiness. By replacing specific steel tubulars with carbon-fiber-reinforced polymer (CFRP) laminated composite structures, different chassis configurations were numerically developed and detailed simulations to compare both masses and mechanical responses were carried out. The paper proves that with this approach it is possible to lighten the chassis up to 9%, while achieving a 7% increase in torsional stiffness and a 9% increase in Specific Energy Absorption (SEA).

Keywords composite materials, crashworthiness, finite element models, load-bearing structures, metal replacement, torsional stiffness

1. Introduction

The last decades represented a period of large scale usage of CFRP composite laminates for the production of high-performance primary and secondary structural components. Examples can be found in military fighter aircraft (Ref 1), civil transport aircraft (Ref 2), helicopters (Ref 3), satellites (Ref 4), and high-speed cars (Ref 5, 6) and motorbikes (Ref 7, 8). The reason for this rapid diffusion is related to the impressive advantages, as well as high stiffness-to-weight and strength-to-weight ratios, fatigue performance, and high tailoring and molding capabilities offered by CFRP composites in regard to the conventional materials.

First employments of CFRP composites date from the 1960s, in aeronautical applications. Here, only small and non-structural components as trim tabs, spoilers and rudders in military aircraft were produced. Only a decade later aircraft manufacturers slowly extended composites to secondary structures in civil applications (Ref 9). Today, as reported in (Ref 10), the leading aircraft manufacturers make an extensive use of composites and the latest model of Boeing B787 has a 50% of composite content for its components, while Airbus A350 reached a 53% of composite content.

This design approach of replacing conventional metal materials with lighter composites with superior mechanical performance is a tangible solution to the ever-evolving needs of the industrial component market, representing an important opportunity to increase product sustainability and competitiveness (Ref 11).

Several literature works show that metal replacement based approaches are particularly helpful in the design of electric vehicles (Ref 12-15). This is because electric motorisation is always associated with the need of significant structural lightening, as the added batteries or electric components make Electric Vehicles (EVs) heavier than conventional Internal Combustion Engine (ICE) vehicles. Indeed, EVs are typically 125% heavier than ICE equivalents. Therefore, weight reduction is mandatory to increase the driving range by using a single battery charge. On average, it is estimated that for an electric vehicle, a 10% reduction in weight is equivalent to a 13.7% increase in range (Ref 11).

The effectiveness in lightweighting related to the use of composite structures as structural components for EVs is demonstrated, for example, in (Ref 14). In this work, the body structure of an EV was redesigned by considering CFRP composite materials. In this way, the authors achieved a weight saving of 28% compared to the conventional structure and

This article is an invited submission to the Journal of Materials Engineering and Performance selected from presentations at the 4th International Symposium on Dynamic Response and Failure of Composite Materials (Draf2022) held June 21–25, 2022, on the Island of Ischia, Italy. It has been expanded from the original presentation. The issue was organized by Valentina Lopresto, Ilaria Papa, Antonello Astarita, and Michele Guida of the University of Naples Federico II.

A. Garofano, V. Acanfora, F. Fittipaldi, and **A. Riccio**, Department of Engineering, University of Campania "L. Vanvitelli", Via Roma, 29, 81031 Aversa, CE, Italy. Contact e-mail: valerio.acanfora@unicampania.it.

consequently an improvement of approximately 38% in driving range.

In this framework, it is possible to consider the present paper. Indeed, it presents a numerical feasibility and effectiveness study in terms of weight saving, and torsional stiffness and crashworthiness enhancement of an electric minibus chassis lightened by replacing steel tubulars with carbon fibers composite laminates. This approach is particularly innovative because, for this category of transport vehicles, structural lightweighting rarely involved the use of collaborative composite structures. Usually, as shown in (Ref 16), attempts to lighten the structure involve processes of optimization and redistribution of chassis tubular thicknesses. Whereas the proposed approach involves the use of composite laminates not only as a means of lightening the chassis, but also as collaborative structures able to improve the mechanical response of the chassis by increasing its torsional stiffness and improving its impact loads' absorbing capabilities.

In detail, to assess the influence of the composite panels on the torsional stiffness of the chassis, the results obtained from a static analysis conducted on the all-steel chassis were compared with those obtained from four configurations in which the positioning of the load-bearing composite structures was varied. In addition, the dynamic mechanical responses of these five (steel or steel-composite) chassis were studied by performing numerical crash test simulations according to the Euro NCAP Full Width Rigid Barrier crash test standard prescription and their ability to handle impact energy was measured with specific energy absorption indexes.

The finite elements chassis' discretization has been performed in Abaqus using a fine formulation that involves C3D8 elements for the tubulars and S4 elements for the composite laminates. The failure mechanisms of the adopted materials have been considered in the numerical analysis as well. In particular, the onset and evolution of the intralaminar damage mechanisms of the composite component have been assessed by using the Hashin's failure criteria; finally, the ductile damage mechanisms of A-36 steel component, which constitutes the chassis' structure, have been considered by introducing the Johnson–Cook criteria.

Mathematical foundations necessary for the implementation of numerical models are introduced in Sect. 2; FE models development and analyses set-ups is provided in Sect. 3; finally, results are discussed and cross-compared in Sect. 4.

2. Theoretical Background

A discussion on the mathematical fundamentals regarding the materials' damage models involved in the numerical simulation is introduced in this section.

In particular, in subSect. 2.1, the numerical approach concerned for the calculation of the ductile damage of the steel chassis is described, while in subSect. 2.2, details about the calculation of the intra-laminar damage onset and evolution of the composite elements are presented.

2.1 Ductile Material Damage Model

Ductile material structures involved in dynamic phenomenon analyses, such as impact phenomena, require to consider the effects of strain rate, deformation and temperature in the numerical estimation of the material response. Many failure model for ductile materials can be found in literature and, in this work, the Johnson–Cook failure model (J-C) has been adopted for the prediction of the material behavior.

In the J–C model, the Von Mises flow stress $\tilde{\sigma}$ can be evaluated as a function of the equivalent plastic strain $\bar{\varepsilon}^{pl}$, equivalent plastic strain rate $\dot{\bar{\varepsilon}}$ and temperature T, according to Eq (1) (Ref 17–19):

$$\bar{\sigma} = \left(A + B\left(\bar{\varepsilon}^{pl}\right)^{n}\right)\left[1 + C\ln\left(\frac{\dot{\bar{\varepsilon}}^{pl}}{\dot{\bar{\varepsilon}}_0^{pl}}\right)\right](1 - T^{*m}) \quad \text{(Eq 1)}$$

A, B, C and m in Eq (1) represent the yield stress of the material, the strain hardening constant, the strengthening coefficient of strain rate, and the thermal softening coefficient, respectively. These are material-related constants; the ratio $\frac{\dot{\bar{\varepsilon}}^{pl}}{\dot{\bar{\varepsilon}}_0^{pl}}$ represents the normalized equivalent plastic strain rate, n identifies the strain hardening exponent. T^* is the homologous temperature and can be evaluated as defined in Eq (2):

$$T^* = (T - T_{\text{room}})/(T_{\text{melt}} - T_{\text{room}}) \quad \text{(Eq 2)}$$

In Eq (2) T represents the material temperature, T_{room} the room temperature, and T_{melt} the melting temperature.

The initiation and the evolution of the dynamic progressive damage was evaluated by using two different J-C criteria. As stated by the J-C mathematical model, the equivalent plastic strain at the onset of damage can be expressed as:

$$\bar{\varepsilon}_D^{pl} = [d_1 + d_2\exp(-d_3\eta)]\left[1 + d_4\ln\left(\frac{\dot{\bar{\varepsilon}}^{pl}}{\dot{\bar{\varepsilon}}_0}\right)\right](1 + d_5T^*) \quad \text{(Eq 3)}$$

In Eq (3) d_1, d_2, d_3, d_4 and d_5 are constant terms related to damage onset, while η represents the ratio between the pressure and the von Mises stress, as stated in Eq (4):

$$\eta = -\frac{p}{\tilde{\sigma}} \quad \text{(Eq 4)}$$

According to the J-C damage onset criterion, failure starts when the D parameter, expressed in Eq 5, is equal to 1.

$$D = \sum \frac{\Delta\bar{\varepsilon}^{pl}}{\bar{\varepsilon}_D^{pl}} \quad \text{(Eq 5)}$$

Once D parameter reaches the limit value, a progressive degradation of the material stiffness is considered as a function of a specified damage evolution law. Abaqus/Explicit takes into account a progressive damage evolution based on the fracture energy, ensuring that the energy dissipated during the damage evolution is equal to the critical strain energy release rate, Gc. In this method, the progressive degradation of material stiffness and the evolution of the damage leads to a material failure when the global damage variable D, expressed in Eq (6), is 1.

$$D = 1 - \exp\left(-\int_0^{\bar{\varepsilon}^{\text{pl}}} \frac{\sigma_y\dot{\varepsilon}^{\text{pl}}}{G_c}\,\text{dt}\right) \quad \text{(Eq 6)}$$

2.2 Intralaminar Damage Model

An elastic-brittle evolution characterize the behavior of the fiber reinforced composite materials and, in literature, many failure criteria and damage evolution models for composites

can be found. In this work, the Hashin's failure criteria and the continuum damage mechanics (CDM) have been used to assess the intra-laminar damage onset prediction and the damage evolution within the laminate, respectively.

According to the Hashin failure theory, separate criteria for detect matrix and fiber failure have been adopted considering the stress components interactions in the orthotropic reference system.

Therefore, four different failure modes and related indexes are considered: longitudinal tension F_{ft} and longitudinal compression F_{fc}, that are related to the stress measured in the longitudinal axis (axis 1 in the orthotropic reference system), which mechanical response is dominated by the fibers; transversal tension F_{mt} and transversal compression F_{mc}, that are related to the stress components evaluated along the transversal axis (axis 2 in the orthotropic reference system), which mechanical response is dominated by the matrix. The following equations introduces the mathematical laws that allows the calculation of these failure modes. (Ref 20, 21):

$$\text{Longitudinal tension } (\sigma_{11} \geq 0)\ F_{ft} = \left(\frac{\sigma_{11}}{X_T}\right)^2 + \alpha\left(\frac{\sigma_{12}}{S_L}\right)^2 = 1 \quad \text{(Eq 7)}$$

$$\text{Longitudinal compression } (\sigma_{11} < 0)\ F_{fc} = \left(\frac{\sigma_{11}}{X_C}\right)^2 = 1 \quad \text{(Eq 8)}$$

$$\text{Transversal tension } (\sigma_{22} \geq 0)\ F_{mt} = \left(\frac{\sigma_{22}}{Y_T}\right)^2 + \left(\frac{\sigma_{12}}{S_L}\right)^2 = 1 \quad \text{(Eq 9)}$$

$$\text{Transversalcompression } (\sigma_{22} < 0)\ F_{mc} = \left(\frac{\sigma_{22}}{2S_T}\right)^2 + \left[\left(\frac{Y_C}{2S_T}\right)^2 - 1\right]\frac{\sigma_{22}}{Y_C} + \left(\frac{\sigma_{12}}{S_L}\right)^2 = 1 \quad \text{(Eq 10)}$$

where σ_{11}, σ_{22} and σ_{12} represent the applied stresses in the orthotropic reference system. X_T, X_C, Y_T and Y_C represent the tensile and compressive strengths in fiber direction and in the matrix direction, respectively; while S_L and S_T represent the longitudinal and transverse shear strengths. The contribution of the shear stress component σ_{12} to the fiber tensile criterion is considered through the α coefficient ($0.0 < \alpha < 1.0$).

As stated by the Continuum Damage Mechanics approach, a bilinear damage evolution law can be associated to the presence of Hashin's failure criteria. The damage evolution law predicts the material degradation in each failure mode taking into account the four fracture energies related to each mode.

A graphic illustration of the onset and evolution of intralaminar composite damage is depicted in Fig. 1. In it, the process of damage initiation is expressed by the OA segment. Indeed, it expresses the undamaged element status, whose stiffness corresponds to the initial one K. Once one of the Hashin damage initiation criterion is met, at location A, a decrease of the stiffness and of the residual strength is followed by the application of further loads. In the degradation phase AB, the stiffness is decreased as a function of the degradation coefficient d_i: a reduced stiffness value K_d characterizes this phase. The stress state of the material in the damaged conditions is computed from:

$$\sigma = C_d \varepsilon \quad \text{(Eq 11)}$$

where C_d is the damaged elasticity matrix, which can be written as:

$$C_d = \frac{1}{D}\begin{bmatrix} (1-d_f)E_1 & (1-d_f)(1-d_m)\nu_{21}E_1 & 0 \\ (1-d_f)(1-d_m)\nu_{12}E_2 & (1-d_m)E_2 & 0 \\ 0 & 0 & (1-d_s)GD \end{bmatrix} \quad \text{(Eq 12)}$$

where $D = (1-d_f)(1-d_m)\nu_{12}\nu_{21}$. The damage variables for fiber failure mode d_f, matrix failure mode d_m and shear failure mode d_s assume the following forms:

$$d_f = \begin{cases} d_f^t \; if\; \sigma_{11} \geq 0 \\ d_f^c \; if\; \sigma_{11} < 0 \end{cases} \quad \text{(Eq 13)}$$

$$d_m = \begin{cases} d_m^t \; if\; \sigma_{22} \geq 0 \\ d_m^c \; if\; \sigma_{22} < 0 \end{cases} \quad \text{(Eq 14)}$$

$$d_s = 1 - \left(1-d_f^t\right)\left(1-d_f^c\right)\left(1-d_m^t\right)\left(1-d_m^c\right) \quad \text{(Eq 15)}$$

Each damage variable for a failure mode is given by the following equation:

$$d_i = \frac{\delta_{eq,i}^f\left(\delta_{eq,i} - \delta_{eq,i}^0\right)}{\delta_{eq,i}\left(\delta_{eq,i}^f - \delta_{eq,i}^0\right)} \quad \text{(Eq 16)}$$

where δ_{eq} is the equivalent displacement for an applied strain referred to a characteristic finite element length L_C, δ_{eq}^0 is the initial equivalent displacement at which the considered failure criteria is met, and δ_{eq}^f is the displacement at which the material is completely damaged.

3. Finite Element Model

In this section, the geometry of the chassis, the discretisation of the mathematical model and the set-up conditions imposed for the numerical investigations are presented. In particular, subsection 3.1 provides a geometric description of the original minibus chassis and its proposed alternative steel-composite hybrid configurations; in subsection 3.2 the discretization approach and the choice of the suitable finite element size are presented; subsection 3.3 describes the set-up conditions adopted to investigate the torsional stiffness of the structure; finally, subsection 3.4 presents the set-up condition to perform the crash test analyses.

3.1 Minibus Chassis Description

In the frame of the present paper, the analyzed structure is fully representative of the chassis of a small electric minibus for public/tourist transport with high efficiency and low environmental impact.

Details on the chassis geometry and dimensions are given in Fig. 2. From the figure, it's possible to note the symmetric structure adopted for this minibus concept. The chassis longitudinal length in the X-direction is 5375 mm and it allows the structure to be classified as representative of a minibus chassis.

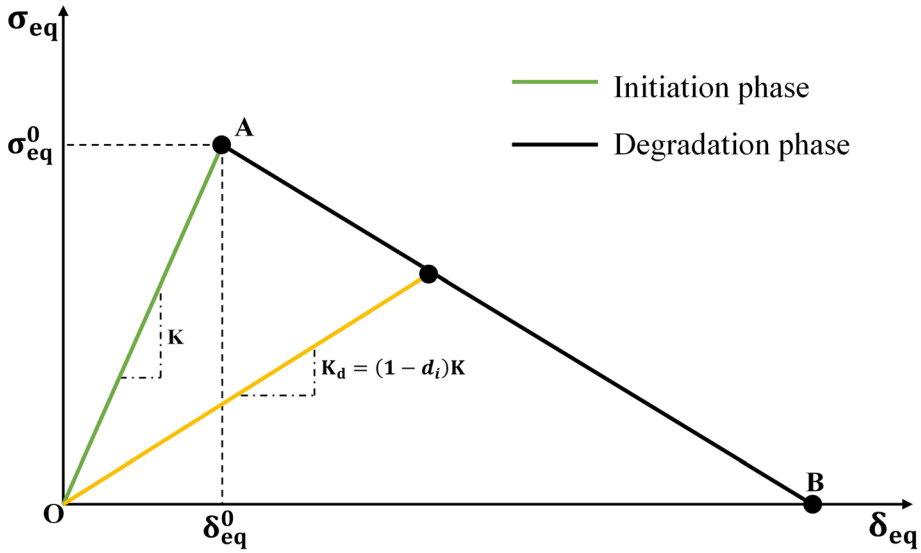

Fig. 1 Bilinear damage evolution law

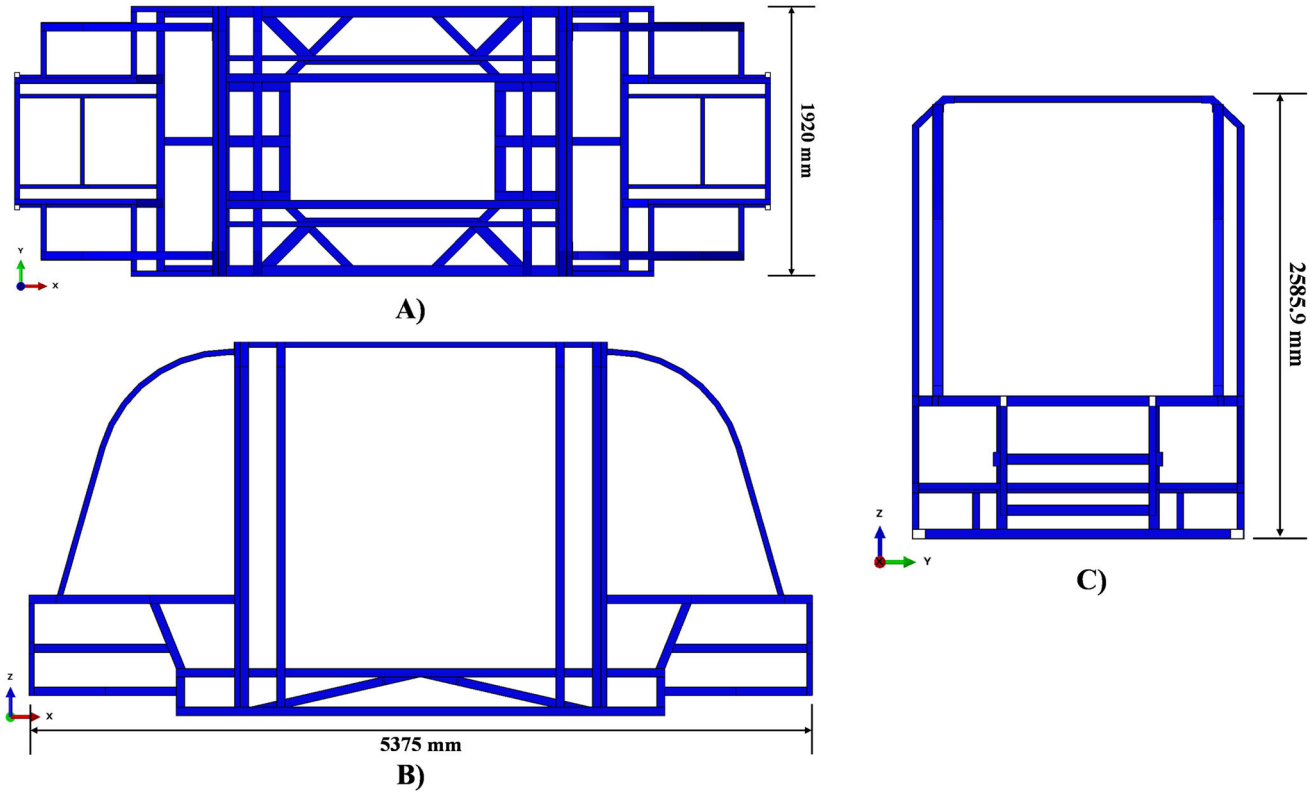

Fig. 2 Chassis geometry and dimensions: (A) top view; (B) lateral view; (C) front view

A detailed chassis FE model has been created in Abaqus. A deformable 3D solid model has been created using rectangular section tubulars with 3D discretization to define each element of the entire structure. Each individual tubular of the whole structure is representative of any structural elements in terms of morphological characteristics, extension and dimensions of the rectangular cross-section. Each individual tubular has been realized as an extrusion body by extruding an appropriate rectangular section along the characteristic axis of the component, as showed in the example of Fig. 3 for a representative tubular elements of the structure.

The assembly of the chassis structure is obtained by positioning each tubular in its planned location adjacent to the surrounding ones. Subsequently, tie constraints have been created between the adjacent elements, simulating the welding of tubulars with adjacent ones.

The material employed for the tubulars in the numerical tool is ASTM A36 steel and its mechanical properties are intro-

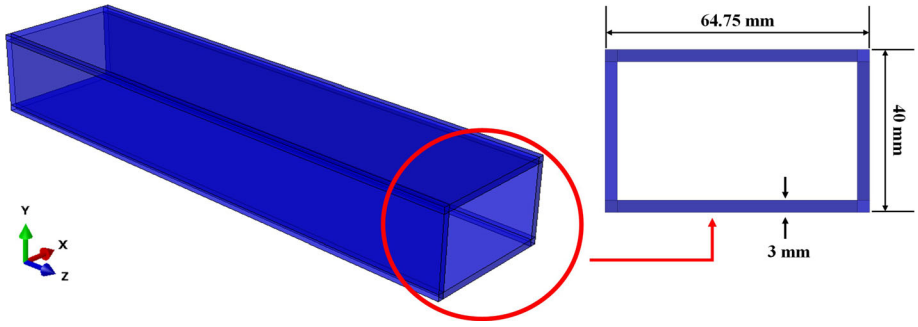

Fig. 3 Example of the chassis tubular elements

Table 1 Mechanical properties of ASTM A36 steel [22]

Property	Value
Density	7890 [kg/m^3]
Young Modulus	200,000.00 [MPa]
Poisson ratio	0.26
Plastic (Nominal)	
Yield stress A	286.10 [MPa]
Strain hardening constant B	500.10 [MPa]
Stress triaxiality η	0.2282
Thermal softening coefficient m	0
Melting Temperature	0
Transition Temperature	0
Rate dependent (Nominal)	
Strain rate strengthening coefficient C	0.0171
$\dot{\bar{\varepsilon}}_0$	1
Johnson–Cook Damage	
d_1	0.403
d_2	1.107
d_3	−1.899
d_4	0.00961
d_5	0.3
Damage evolution	
Fracture energy	12 [kJ]

duced in Table 1 (Ref 22). Specifically, the data required by the solver to measure the ductile fracture of steel using the Johnson–Cook theory (introduced in Sect. 2.1) are A, *B*, *C* and *m*, that identify the yield stress of the material, the strain hardening constant, the strengthening coefficient of strain rate, and the thermal softening coefficient, respectively, and and d_1, d_2, d_3, d_4 and, d_5 that are damage model constants.

Starting from the described geometry, five chassis configurations have been developed by integrating in focused locations of the structure four different composite panels layouts as structural elements. These are depicted in Fig. 4. Each of these configurations is identified with a name as *Chassis N*. In details:

- Chassis 0 identifies the all-steel structure, without composite panels (Fig. 4A);
- In Chassis 1, the steel tubulars of the minibus floor were replaced by a laminated composite panel (Fig. 4B). In this way, an 8.5% lightening of the original configuration was achieved.
- In Chassis 2, a laminated composite panel has been added to the previous configuration in the roof area (Fig. 4C). In this configuration, there is no structural lightening (because the tubulars have not been replaced), but the upper composite panel has been added because, as will be seen in subsection 4.1, it plays a key role in torsional stiffness.
- In Chassis 3, four laminated composite panels have been added to the previous configuration (Chassis 2) in the forward and rear corner areas, replacing four steel tubulars previously present in that areas (Fig. 4D). This resulted in a mass saving of 8.8% compared to the Chassis 0 configuration.
- In Chassis 4, a laminated composite panel has been added to the previous configuration in the lower-forward area of the structure, between the front chassis and the safety cage (Fig. 4E) able to better manage the energy produced during the crash test.

All the laminated composite panels considered in the four configurations were modeled in Abaqus as *1 mm* thickness 3D deformable planar shell parts with a $[90,0,-45,45]_s$ stacking sequence. For all composite laminate panels, a single-ply formulation has been adopted, with a single element in the thickness. Details on the geometry and dimensions of the composite panels are given in Fig. 5.

The composite material considered for the previous components is the IM7/977–2 carbon-fiber reinforced polymer. Its mechanical properties are introduced in Table 2 (Ref 23).

3.2 Finite Elements Discretization and Sensitivity Analysis

The developed 3D model allows a detailed representation of the chassis structure and its geometric characteristic. Consequently, a detailed structured discretization approach with three-dimensional finite elements was used for the chassis structure. In particular, as showed in Fig. 6, the chassis structure was discretized using C3D8 elements, while S4 elements were adopted for the composite panels. The former are 8-node linear brick elements with a full integration scheme, while the latter are 4-node doubly curved general-purpose shell elements with full integration scheme. The use of full integration scheme elements in discretizing steel frames and composite panels allowed to avoid completely the absorption of energy through hourglass phenomena.

Linear static analyses have been conducted to define the size of the finite elements relating the solution accuracy to the computational cost. Two reference points have been created in the forward zone and in the rear zone of the chassis in order to assign to the front axle and to the rear axle the boundary conditions. Two coupling constraints linked the reference points to the front axle points and to the rear axle points,

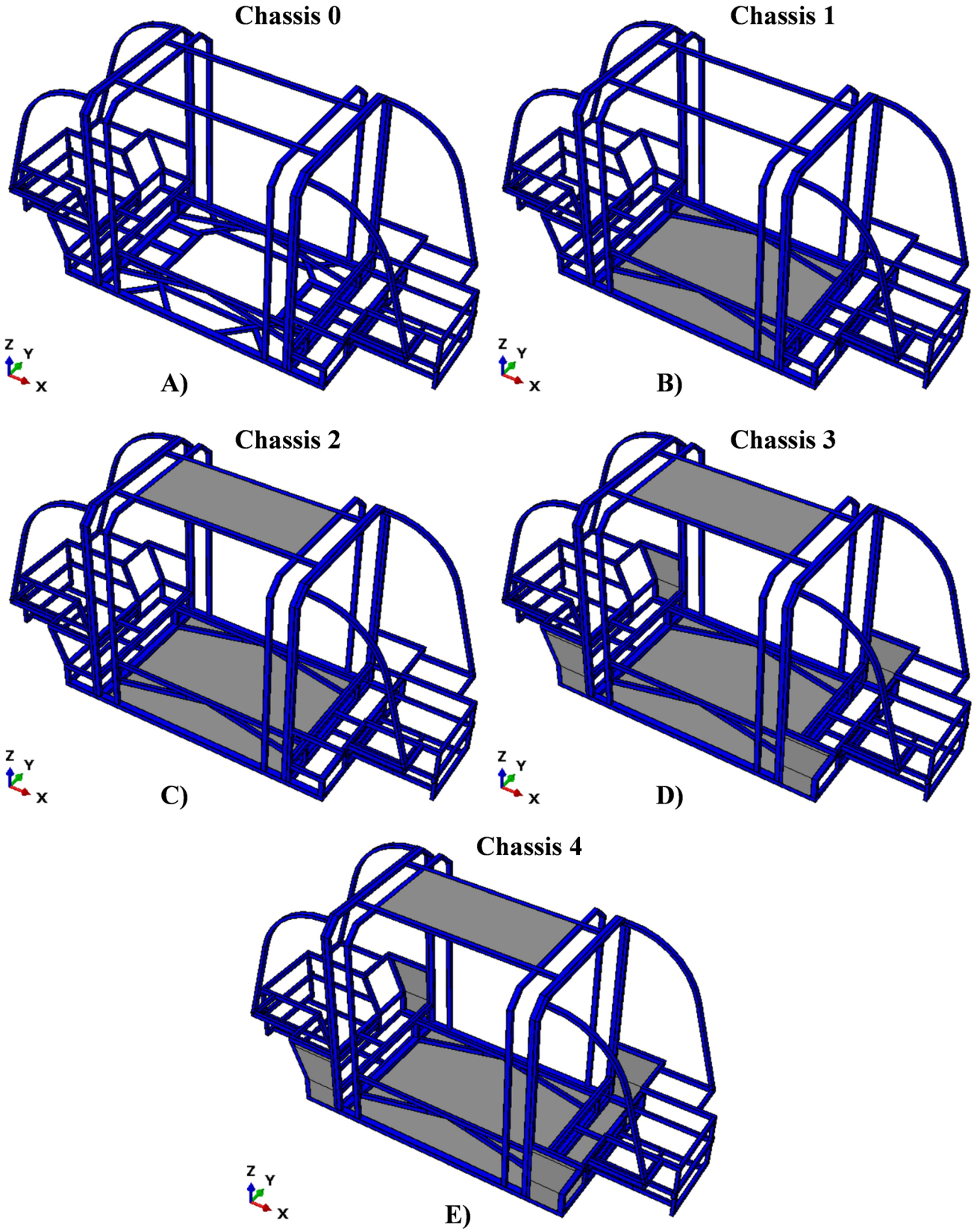

Fig. 4 Chassis configurations: (A) Chassis 0; (B) Chassis 1; (C) Chassis 2; (D) Chassis 3; (E) Chassis 4

respectively. Analyses have been performed clamping the rear wheel axle and applying a 5 mm traction displacement to the front wheel axle, as showed in Fig. 7.

The comparison in terms of Von Mises Sigma (Fig. 8A) and computational time (Fig. 8B) has been reported as a function of the tested chassis finite element sizes. The maximum calcula-

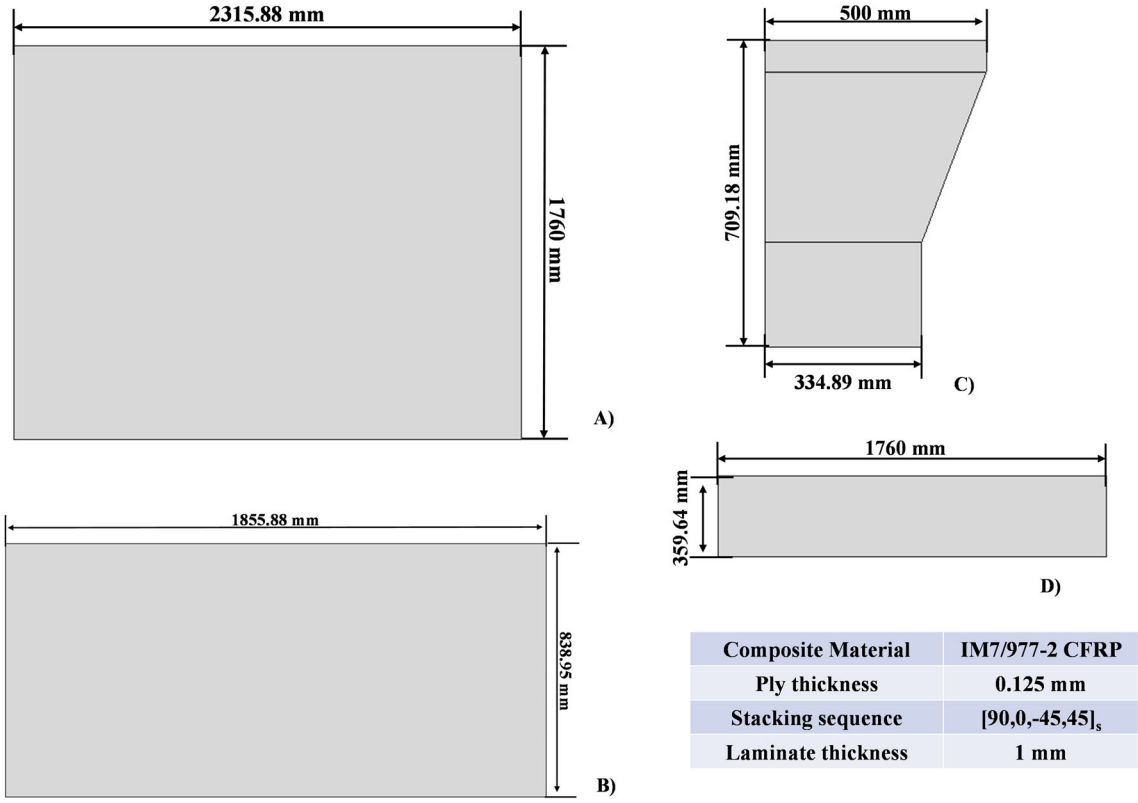

Fig. 5 Composite panels geometry and dimensions: A) floor panel; B) roof panel; C) corner panel; D) floor forward panel

Table 2 Mechanical properties of IM7/977–2 [23]

Property	Value
Ply thickness	0.125 mm
Stacking sequence	$[90,0,-45,45]_s$
Density	1400 [kg/m^3]
E_1	153,050 MPa
$E_3 = E_2$	10,300 MPa
$G_{12} = G_{13}$	6000 MPa
G_{23}	3700 MPa
$\nu_{12} = \nu_{13}$	0.30
ν_{23}	0.42
Hashin Damage	
Longitudinal Tensile Strength X_T	1250 MPa
Longitudinal Compressive Strength X_C	850 MPa
Transverse Tensile Strength Y_T	65 MPa
Transverse Compressive Strength Y_C	200 MPa
Longitudinal Shear Strength S_L	75 MPa
Transverse Shear Strength S_T	35 MPa
Damage evolution	
Longitudinal Tensile Fracture Energy	15 kJ/m^2
Longitudinal Compressive Fracture Energy	7 kJ/m^2
Transverse Tensile Fracture Energy	0.5 kJ/m^2
Transverse Compressive Fracture Energy	4 kJ/m^2

tion time was used to scale the time comparison, avoiding the machine dependency from the evaluation.

As showed in the comparison in Fig. 7, the performed mesh sensitivity analyses demonstrated that elements with a length smaller than 10 mm does not improve the solution in terms of stresses. On the other hand, reducing the elements' length below 10 mm produces an increase in computational time.

Therefore, the chassis is discretized with 10 mm size elements.

3.3 Torsional Stiffness Determination Analysis Set-Up

The torsional stiffness of an automotive chassis can be evaluated by considering a torsion condition on the structure. A known torque can be applied to the chassis structure by using actuators fixed to the chassis in a point near the forward suspension pick-up points. Simultaneously, the rear suspension spring mounts are fixed to the ground by using rigid fixtures.

During the test, dial gauges are used to measure the displacement at the point in which the actuators are fixed to the chassis structure. Torsional stiffness K_T (Nm/degree) of the chassis can be calculated as stated in Eq (17):

$$K_T = \frac{M_T}{\theta} \quad \text{(Eq 17)}$$

where M_T (Nm) is the known applied torque and θ (degree) represents the twist angle. The twist angle can be calculated by using the collected displacement data δ (m) as stated in Eq (18):

$$\theta = 2 * \frac{|\delta|}{d} * \frac{180}{\pi} \quad \text{(Eq 18)}$$

where d (m) represents the distance between the left and right supports.

In order to numerically simulate the torsional test and evaluate the torsional stiffness of the several minibus chassis configurations, linear static analyses have been performed applying to the structure the boundary conditions showed in Fig. 9. The rear wheel axle has been clamped while a 2000 Nm

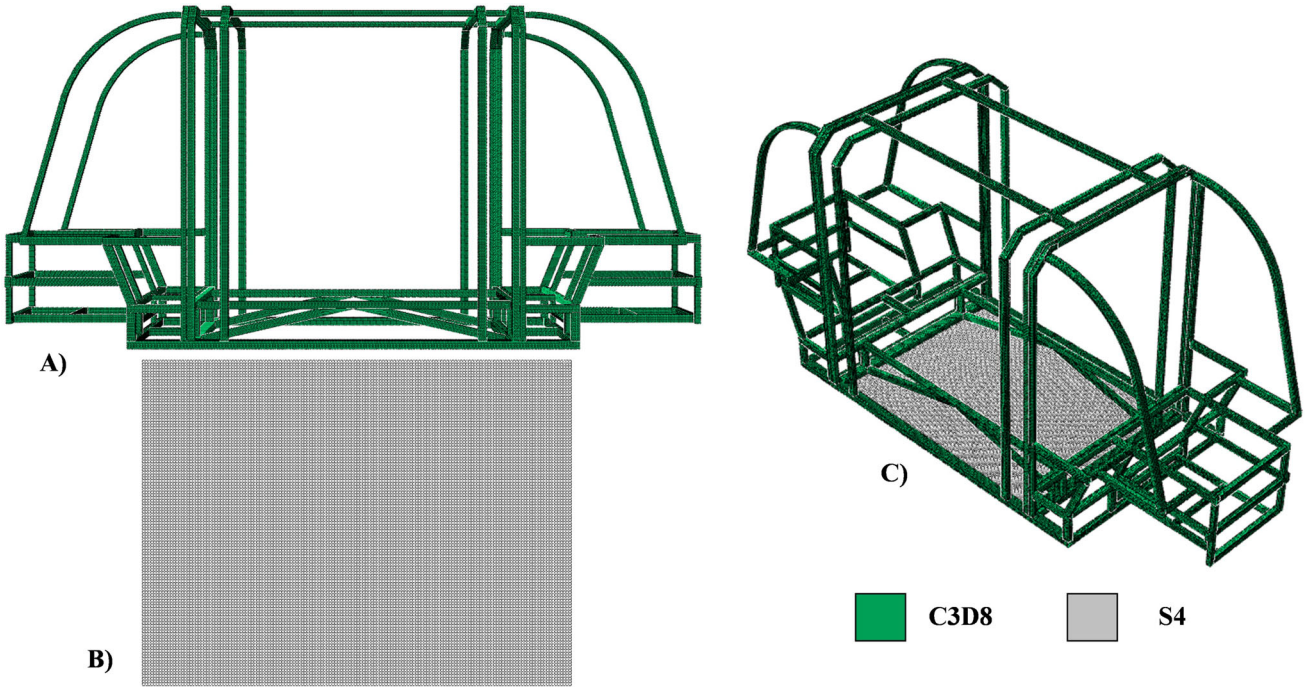

Fig. 6 Chassis 1 finite element discretization: (A) Steel chassis; (B) Composite laminate panel in the floor area; C) Whole hybrid chassis structure

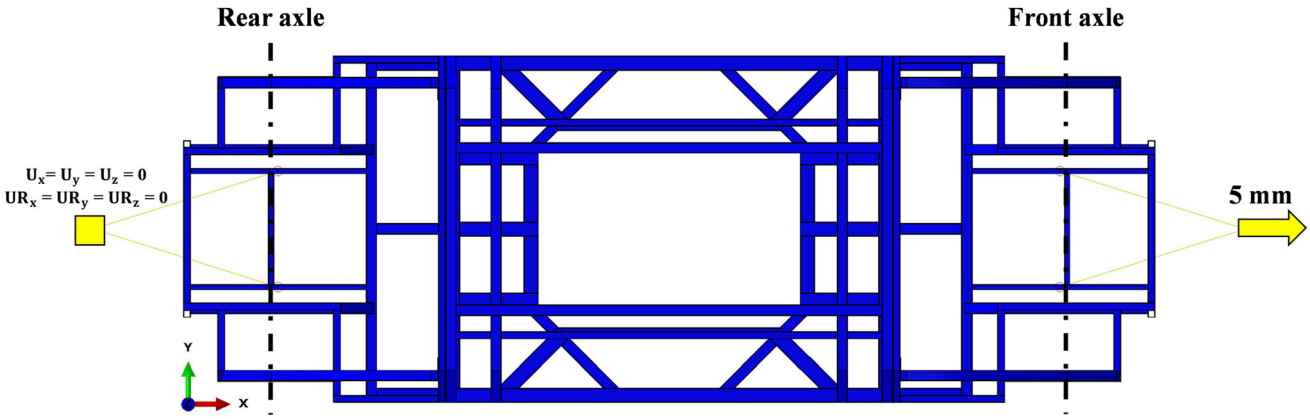

Fig. 7 Sensitivity analyses boundary conditions

torque was applied to the front wheel axle. Static linear analyses have been performed for all the configurations to investigate the mechanical behavior of the structure in a torsional condition.

3.4 Crash Test Set-up

The crashworthiness of the proposed chassis has been evaluated performing Full Width Rigid Barrier crash tests configured according to EuroNCAP standard. Therefore, a rigid barrier was implemented adding to the assembly a rectangular 3000 × 2500 × 100 mm solid extrusion part, while a 7000 × 3000 mm rectangular planar shell part simulates the presence of a reference road. The rigid barrier and the road have been discretized by using C3D8R elements and S4R elements, respectively. Furthermore, both the road and the rigid barrier were considered as rigid bodies and all their degrees of freedom were locked.

According to the adopted standard prescription, an impact speed (along the X-direction) of 50 km/h has been assigned to the chassis. By defining the gravitational acceleration, the numerical simulations consider the gravitational effect. The crash test set-up adopted as boundary conditions for the analyses is introduced in Fig. 10.

4. Numerical Results

The effects of introducing laminated composite panels as structural elements in the chassis of the minibus are discussed in this section. In particular, subsection 4.1 discusses the improvements in terms of torsional stiffness and mass reduction, while subsection 4.2 analyses the impact responses of the chassis in full frontal crash tests.

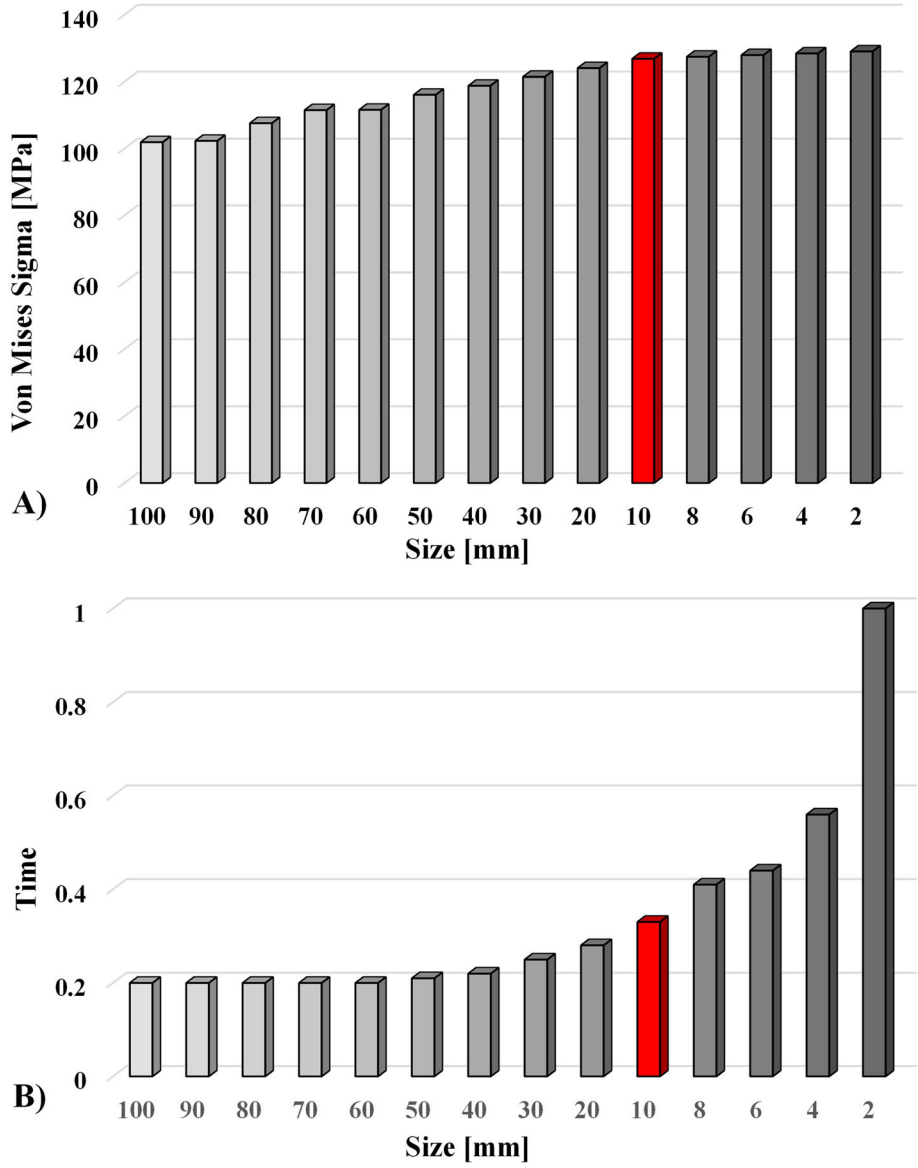

Fig. 8 Sensitivity analyses remarks: (A) Stress comparison; (B) CPU time comparison

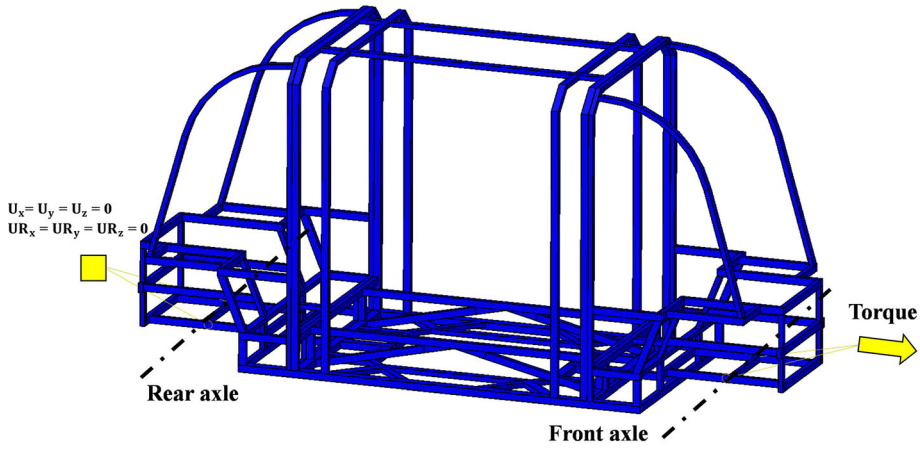

Fig. 9 Analysis set-up for the determination of the chassis torsional stiffness

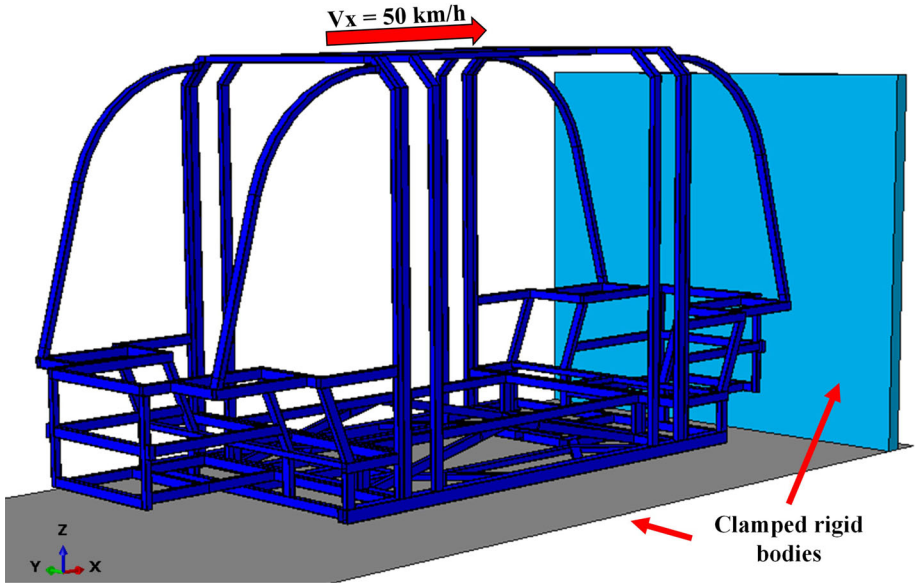

Fig. 10 Full Width Rigid Barrier crash test standard prescription

4.1 Torsional Stiffness and Mass Reduction Investigation

The static analyses performed in Abaqus/Standard on the five considered configurations of the chassis allowed to investigate the effect of the composite panels on the torsional mechanical performances of the structure and estimate the torsional stiffness of the chassis by using the approach presented in the subsection 3.3. In Fig. 11, the displacement in z-direction of the five chassis configurations is presented. These results are introduced in both isometric and frontal views in order to highlight the θ angle, which, according to the theory presented in Sect. 3.3, allows to compare the torsional stiffness of the chassis.

As showed, with respect to the Chassis 0, the presence of the laminated composite panels as load-bearing structures in specific location of the chassis makes possible to reduce the torsion of the structure with a subsequently increase in the torsional stiffness K_T. In detail, in Chassis 0 the torsion angle is calculated as 0.5851°, while in Chassis 4 the presence of the composite panels in key locations of the chassis reduced the torsion angle to 0.5431, with a decrease of 7%.

Moreover, a significant reduction in mass of the whole structure can be recorded. Data in Table 3 and histogram graphs in Fig. 12 highlight the mentioned benefits. The Chassis 1 configuration represents a particular case in which a slight reduction (roughly 1%) in torsional stiffness with respect to the initial configuration is acceptable because it is followed by a reduction in the total mass of the structure around 8%. Both the Chassis 2 and Chassis 3 configurations represent cases in which the reduction in mass is combined with an increase in torsional stiffness, due to the focused positioning of the load-bearing composite panels.

In the Chassis 4 configuration with respect to the Chassis 3, the elimination of a tubular in the area between the front chassis and the safety cage and the subsequent positioning of an additional composite panel in that area allows a further increase in torsional stiffness, without affecting the total mass of the structure. The adopted composite panel is characterized by an equivalent mass as the eliminated tubular but it provides a greater contribution in terms of torsional stiffness.

With respect to the all-steel Chassis 0 configuration, the Chassis 4 is characterized by a reduction in the total mass of the structure around 9% (Fig. 12A) and an increase in torsional stiffness around 8% (Fig. 12B). The use of the lightweight composite panels as load-bearing structures demonstrated to be an effective way to improve to torsional mechanical performances of the chassis with a considerable positive effect on the global mass of the structure and consequently on the autonomy of the electric minibus. On average for electric vehicles it has been estimated that a mass reduction of 10% can result in a driving range extension of 13.7% (Ref 11). With this trend, in Chassis 4, a structure mass reduction of 8.8% with respect to Chassis 0 will result in a driving range extension up to 12%.

4.2 Crash Test Results Analyses

The dynamic explicit analyses performed in Abaqus/Explicit on the five considered configurations of the chassis allowed to investigate the effect of the composite panels on the mechanical performances of the chassis when involved in a full frontal crash test against a rigid wall. In particular, the advantages of introducing laminated composite panels as load-bearing elements in the chassis of the minibus are assessed through a comparison in terms of Von Mises stresses, energy absorption features, intralaminar composite damages and length of the chassis at the end of the crash.

The comparison starts with Fig. 13, where the Von Mises stress state on the steel structure of the five configurations at the end of the crash are cross-compared.

Compared to chassis 0, there is an increase close to 9% in the Von Mises stress state concentrated in all the composite reinforced areas. This is an effect of the composite stiffening. However, as will be demonstrated in the following comparisons, the adoption of composite panels induces a significant improvement in the absorption of impact energy. This is because, through the onset and propagation of intralaminar damage, a substantial amount of impact energy can be dissipated.

A comparison of the damage state of steel tubulars by means of the adopted Johnson–Cook criterion is given in Fig. 14. For all configurations, the majority of the failures have been found

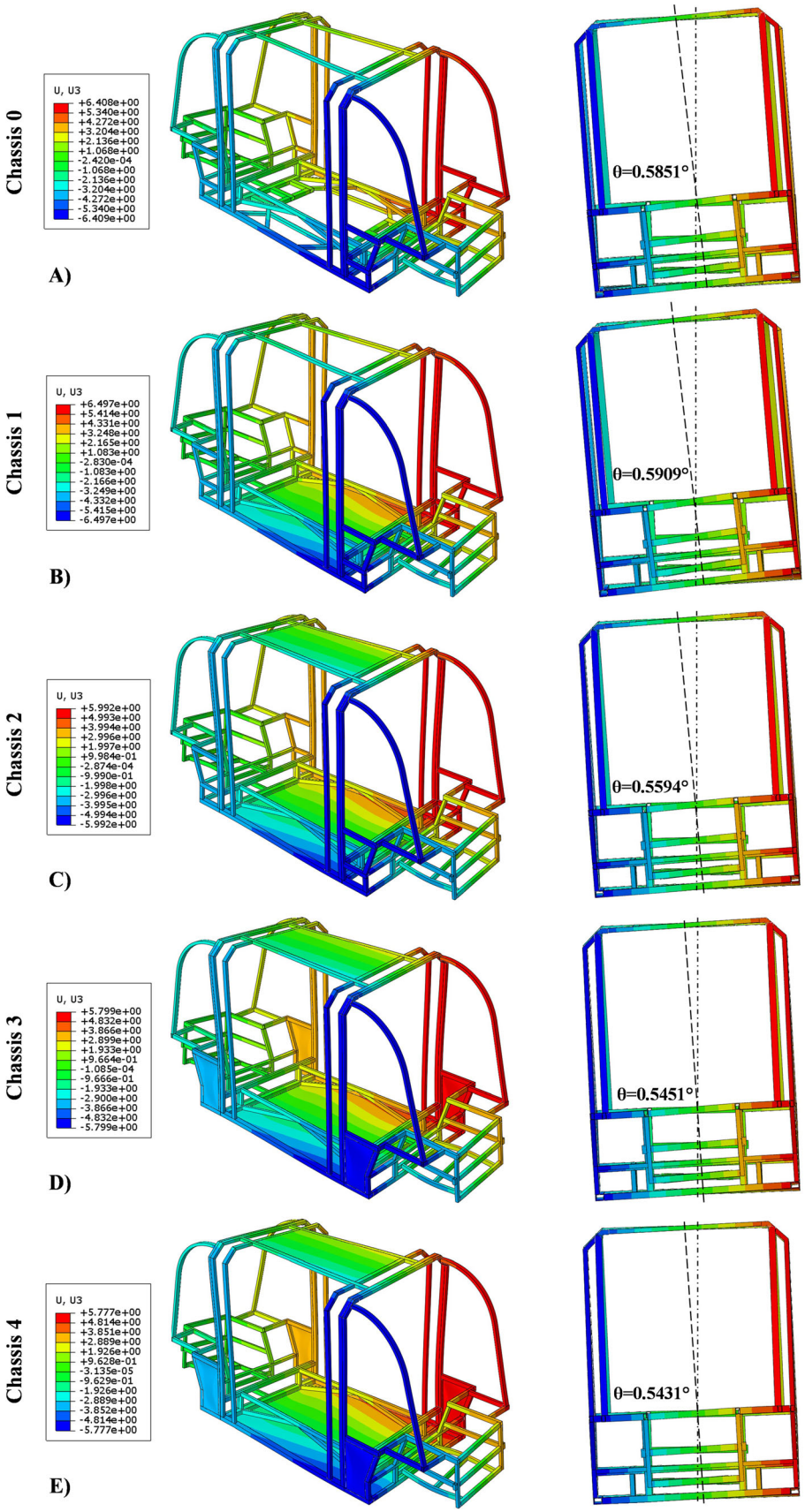

Fig. 11 Chassis displacement in Z-direction in isometric and frontal views: (A) Chassis 0; (B) Chassis 1; (C) Chassis 2; (D) Chassis 3; (E) Chassis 4. (*Note*: An amplification of 12 has been used)

in the front section of the chassis, which is mainly involved in the impact event. The welding points between different tubulars resulted among the most critical points for failures. As illustrated in Fig. 14, Chassis 0 to Chassis 2 configurations are globally the most widespread damaged in the frontal area as the steel components are the only ones to absorb the impact energy through plastic deformation and fracture. In Chassis 3 and Chassis 4 configurations the composite laminate panels contributed to absorb part of the impact energy through the onset and propagation of intralaminar damages, globally reducing the extent of the failures of the steel components. However, the composite panels added in Chassis 3 and 4 induce local stiffening that causes minor failures of its surrounding regions.

The front section of the chassis is the part tuned to absorb the impact energy and provides the larger deformations.

As compared to previous chassis configuration, in Chassis 4 the deformation of the lowest part of the structure varies due to the replacement of the tubular in that area by means of the composite panel which is totally involved in the impact response. In consideration of the large deformations, the composite panel added in that area of the structure by replacing a pre-existing tubular, provided a solution able to stiff the structure and, simultaneously, absorb the impact energy through intralaminar damages.

For all the configurations characterized by the presence of load-bearing composite structures, the damage state of the panels at the end of the impact has been investigated. The intralaminar damage state of the composite panels in Chassis 3 and Chassis 4 is reported in Fig. 15. As the composite panels have been discretized with only one element in the thickness, the reported damage state is representative of the damage envelope across all plies. The composite panels collaborate in the dissipation of the impact energy through the onset and propagation of intra-laminar damages. In particular, in the Chassis 1 and Chassis 2 configurations, the damage state of the panels is negligible, since they are placed further away from the impact area. Nevertheless, they cooperate in the stiffening of the chassis with a huge reduction of the structure's mass and in guaranteeing the ability of the structure to protect its occupants.

Indeed, in the Chassis 3 and Chassis 4 configurations, the contribution provided by the forward composite panels in absorbing the impact energy is evident by observing their damage state in all fiber and matrix damage modes.

From an energy point of view, further comparisons can be performed to better understand the effect of the load-bearing composite panels on the mechanical performances of the chassis involved in a crash test phenomenon. The ratio between the energy absorbed by the whole structure and the total impact energy can be evaluated and higher values represent better results in terms of energy absorption. The greater the amount of total energy absorbed through deformations and failures of steel and composite components, the lower the impact energy perceived by passengers in the safety cage. As showed in the histogram graph in Fig. 16A, the structure in Chassis 0 configuration absorbed 79.11% of the total impact energy, while in Chassis 4 configuration the adoption of composite panels, their influence on the chassis mechanical behavior and the damages that occur in response to the impact provided a gain in the ratio of absorbed energy up to 86.87%.

Moreover, to assess the benefit achieved in terms of reduction of the energy transferred to the passengers, the Specific Energy Absorption (SEA) features have been evaluated in the histogram graph in Fig. 16B. In Chassis 0 configuration, SEA of the all-steel structure was evaluated in 7.63 kJ/kg. Indeed, in Chassis 4 configuration, the employment of a hybrid composite-steel structure increased SEA value to 8.38 kJ/kg. Hence, the adoption of composite panels as load-bearing elements and the definition of a steel-composite hybrid configuration made possible a 10% increase in the structure's effectiveness of absorbing the impact energy, resulting in a benefit for passengers.

Therefore, the introduction of the composite panels increased the structure's efficiency in absorbing the impact energy, reducing the energy transferred to the passengers and the total mass of the chassis. An amount of the impact energy has been dissipated through the onset and propagation of intralaminar damages in the composite panels. In Fig. 17, a comparison

Table 3 Comparison of the chassis configuration in terms of torsional stiffness and mass

Configuration	Twist angle	Torsional stiffness	Mass
Chassis 0	0.5851 deg	3418.2 Nm/deg	658 kg
Chassis 1	0.5909 deg	3384.9 Nm/deg	602 kg
Chassis 2	0.5594 deg	3575.1 Nm/deg	604 kg
Chassis 3	0.5451 deg	3669.1 Nm/deg	600 kg
Chassis 4	0.5431 deg	3682.9 Nm/deg	600 kg

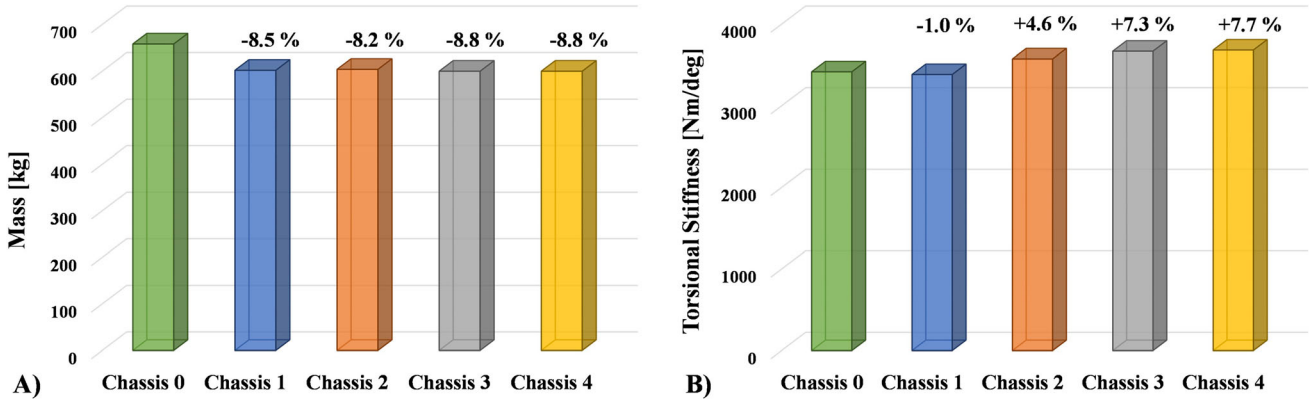

Fig. 12 Comparison of mass and torsional stiffness for the analyzed chassis configurations: (A) Mass comparison; (B) Torsional stiffness comparison

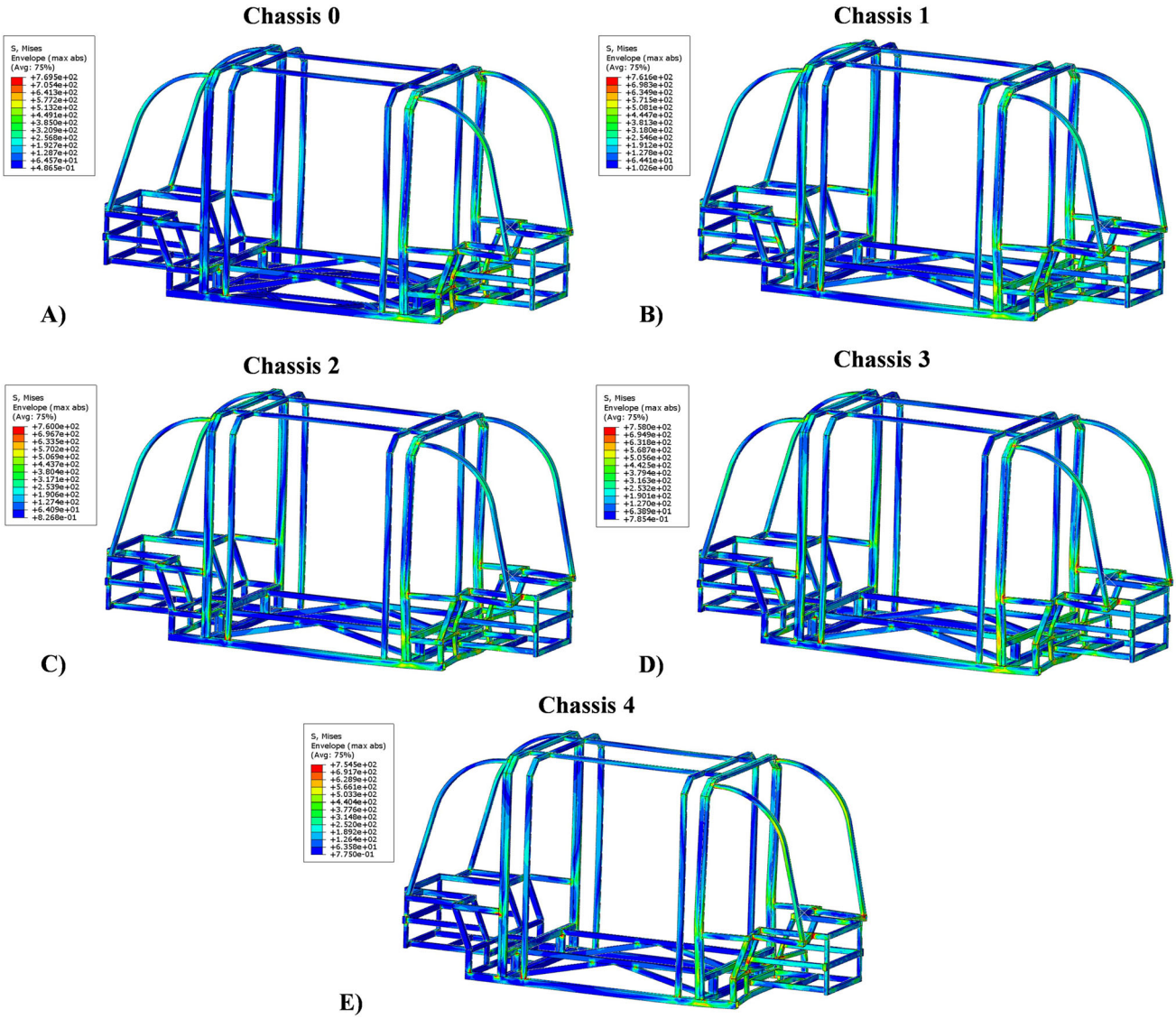

Fig. 13 Von Mises stress state at the end of the impact: (A) Chassis 0; (B) Chassis 1; (C) Chassis 2; (D) Chassis 3; (E) Chassis 4

between the energy absorbed by the composite panels in the different chassis configuration has been performed. As showed in the histogram graph, the energy absorbed by the composite panels in Chassis 1 and Chassis 2 is quite negligible due to the absence of wide intralaminar damages. In Chassis 3, intralaminar damages in the forward corner composite panels (as shown in Fig. 15A) are able to absorb an amount of energy around 0.35 kJ. In Chassis 4, the widespread intralaminar damages in the composite panels (as shown in Fig. 15B) are able to absorb an amount of energy around 1.3 kJ.

In order to verify the stiffening effect of the load-bearing composite panels adopted as a replacement of some steel tubulars in the chassis structure, a comparison of the chassis length before and after the impact has been performed. The reference length in the lengthwise direction of the minibus, as previously shown in Fig. 2B and provided in Table 4 is 5375 mm in the undeformed structure. After the impact, the measured length in the Chassis 0 is 5246 mm with a delta length around 120 mm. Instead, in the Chassis 1 and Chassis 2 the measured length after the impact is 5276 mm with a delta length around 99 mm, while in the Chassis 3 and Chassis 4 the measured length after the impact is 5272 mm and 5265 mm with a delta length of 103 mm and 110 mm, respectively. Therefore, in addition to the aforementioned mass reduction, the replacement of the steel tubulars by means of the composite panels as load-bearing structures demonstrated to stiff the structure at least as the steel tubulars with a slightly increase in the length of the chassis after the impact and ensuring to protect the passengers.

4.3 Numerical Analyses Remarks

All the benefits related to the use of composite panels as load-bearing structures in the chassis highlighted by the performed numerical analyses are summarized in Table 5.

As compared to Chassis 0, in the Chassis 1 configuration the adopted composite panel provides an 8.5% reduction in the total mass of the structure with a slight reduction of the torsional stiffness. This condition is however acceptable thanks to the mass reduction and the stiffening effect on the structure that allows a consequently slight increase in the post-impact chassis length.

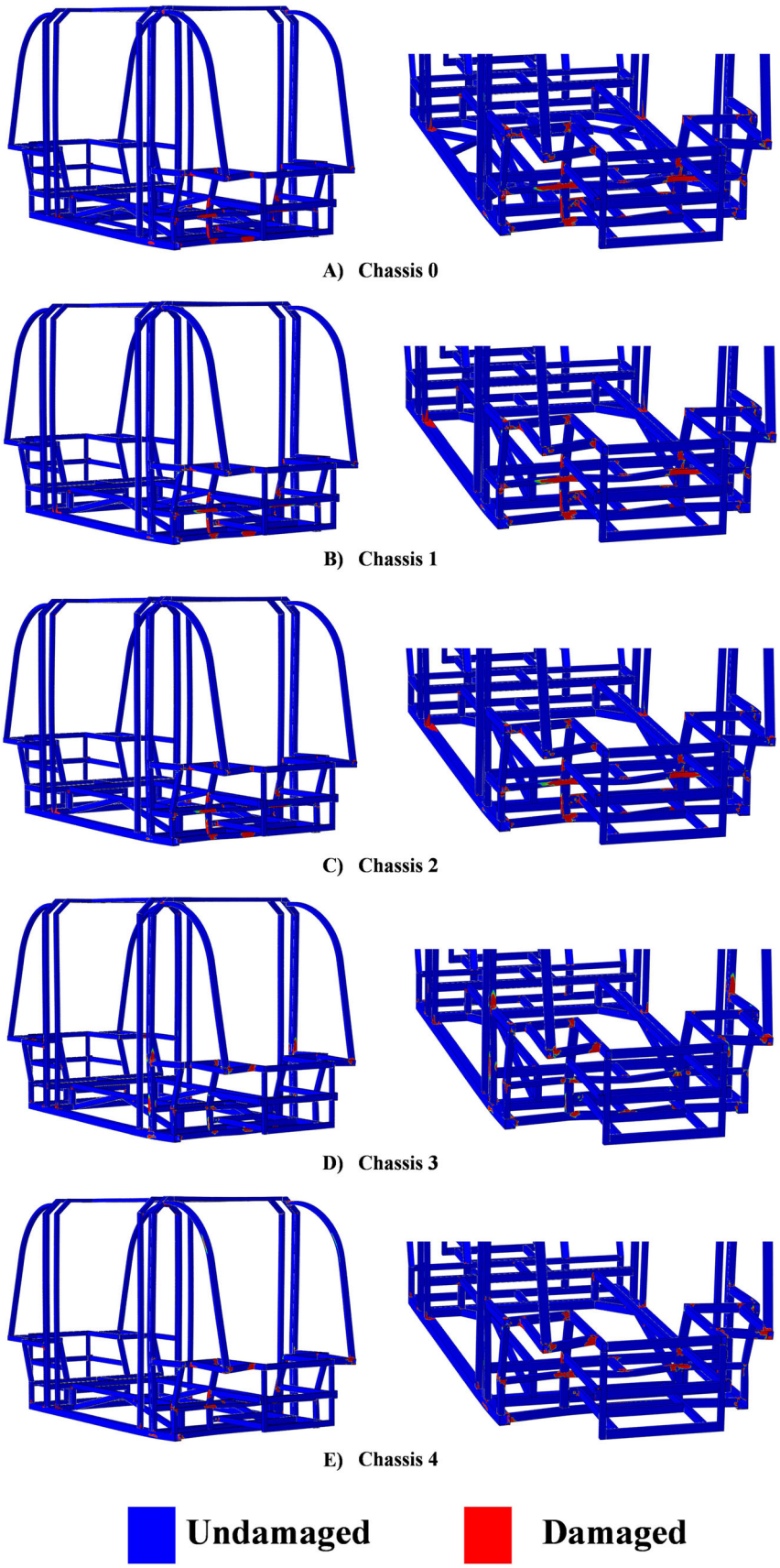

Fig. 14 Damage state at the end of the impact: (A) Chassis 0; (B) Chassis 1; (C) Chassis 2; (D) Chassis 3; (E) Chassis 4

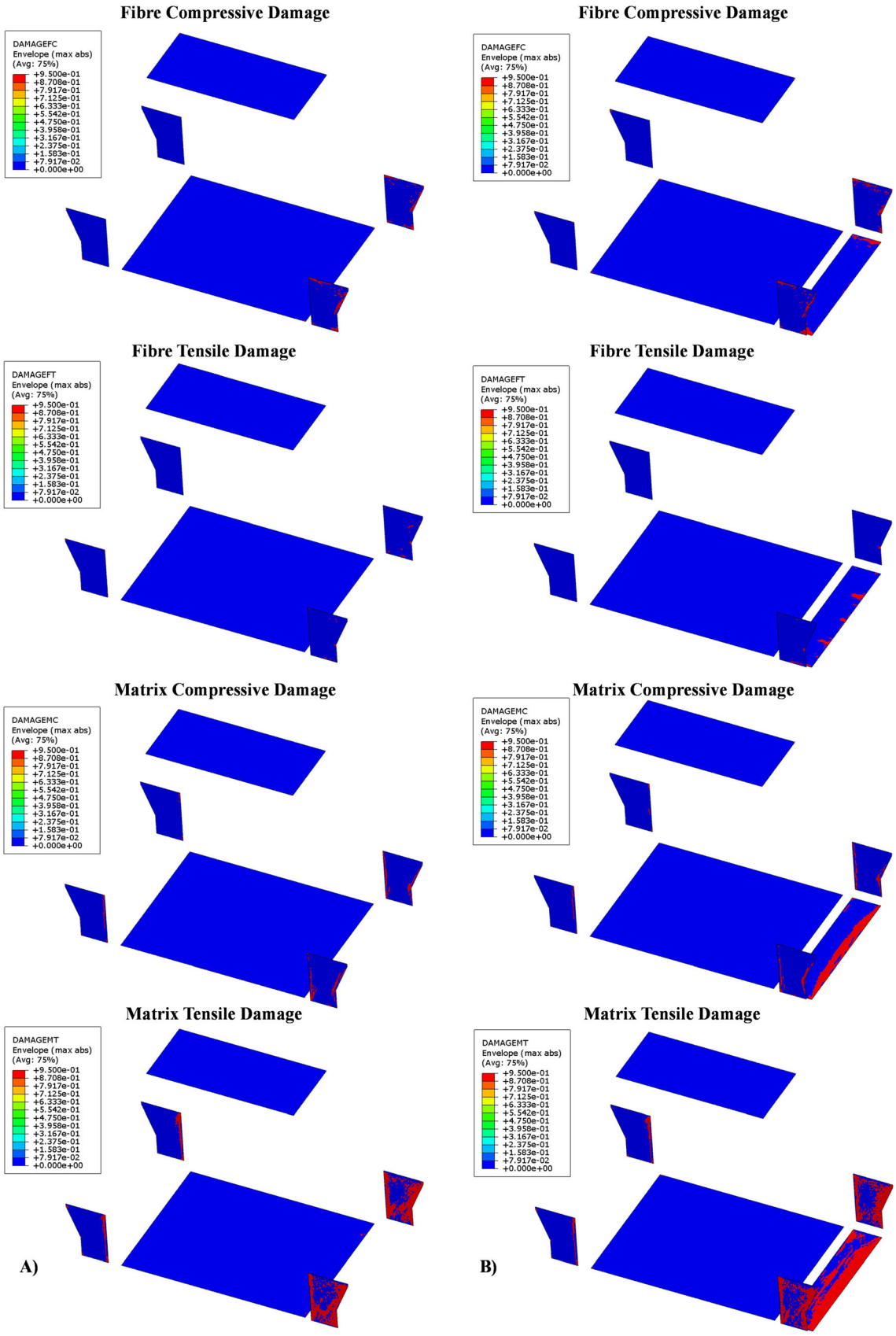

Fig. 15 Intra-laminar damage state of the composite panels in: (A) Chassis 3; (B) Chassis 4

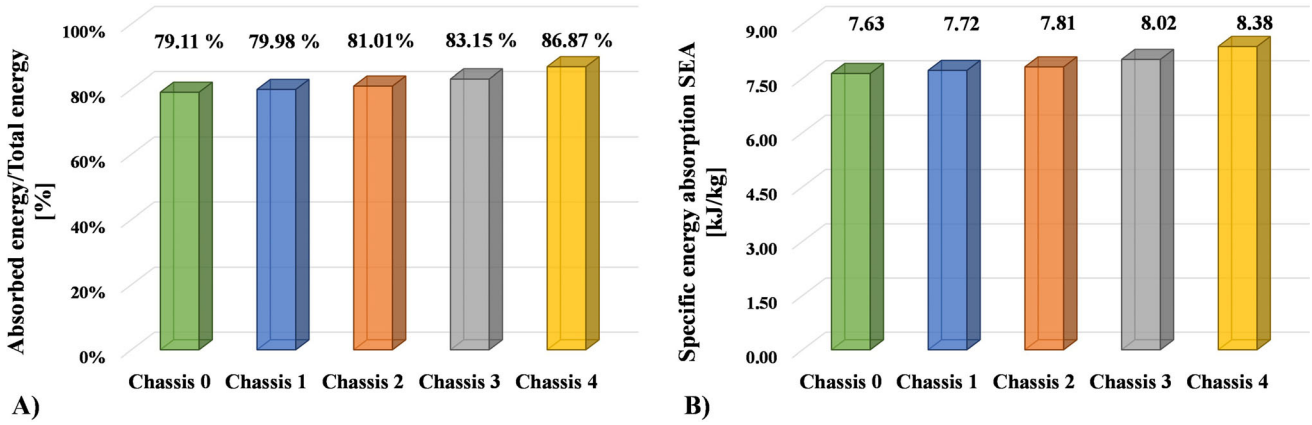

Fig. 16 Energy comparison: (A) Absorbed/Total energy ratio; (B) Specific energy absorption SEA

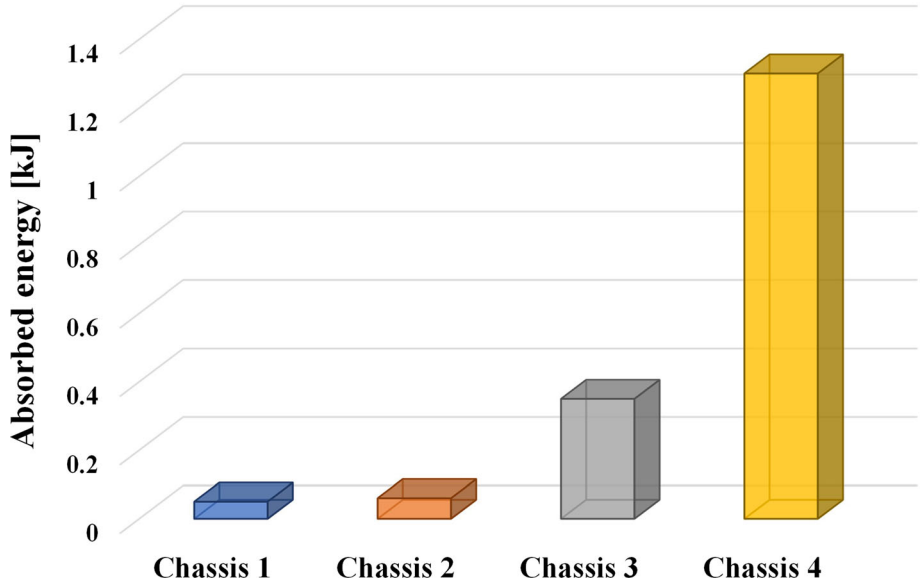

Fig. 17 Comparison of the energy absorbed by composite panels

Table 4 Comparison of the chassis length after the impact

Configuration	Length	Δ length
Undeformed reference	5375 mm	
Chassis 0	5255 mm	120 mm
Chassis 1	5276 mm	99 mm
Chassis 2	5276 mm	99 mm
Chassis 3	5272 mm	103 mm
Chassis 4	5265 mm	110 mm

As compared to Chassis 0, in the Chassis 2 configuration the adopted composite panel layout provides an 8.2% reduction in the total mass of the structure with an increase in the torsional stiffness. With respect to Chassis 1, the composite panel in the roof area of the structure allows to increase the torsional stiffness of the structure with a slight and acceptable increase in the total mass. The stiffening effect on the structure performed by the composite panels is retained as the post-impact chassis length is unchanged.

Both Chassis 3 and Chassis 4 represent configurations in which the trend in mass reduction, torsional stiffness increase and stiffening effect of the chassis is upheld. A maximum 8.8% in mass reduction and a maximum 7.7% in torsional stiffness increase is reached in Chassis 4. Moreover, the contribution provided by the forward composite panels in absorbing the impact energy can be appreciated. The onset and propagation of intralaminar damages were able to absorb a maximum amount of energy of 1.3 kJ. The adoption of the composite panels and the damages that occur in response to the impact produce an increase in the ratio between the energy absorbed by the whole structure and the total energy. In the Chassis 4 configuration, a gain in the ratio of absorbed energy of more than 7% as compared to Chassis 0 has been recorded.

5. Conclusions

Satisfactory torsional stiffness and crashworthiness represent key aspects in the evaluation of the mechanical performances of the chassis structure of a vehicle. Moreover, low

Table 5 Chassis configuration comparison

Configuration	Mass, kg	Torsional Stiffness, Nm/deg	Absorbed energy in composites panels	Absorbed energy ratio, %	Post-impact chassis length, mm
Chassis 0	658	3418.2	…	79.11	5255
Chassis 1	602	3384.9	0.05 kJ	79.98	5276
Chassis 2	604	3575.1	0.06 kJ	81.01	5276
Chassis 3	600	3669.1	0.35 kJ	83.15	5272
Chassis 4	600	3682.9	1.3 kJ	86.87	5265

weight plays a key role in the development of an attractive chassis configuration when fuel consumption and extension of the driving range is taken into account.

The present paper investigates the effectiveness, in terms of torsional stiffness, crashworthiness and mass reduction, of introducing in focused location of the chassis some laminated composite panels as a replacement of the previously existing steel tubulars.

Staring from an all-steel chassis configuration, named Chassis 0, further four configurations have been developed and analyzed numerically simulating a torsion test and a crash test against a rigid wall. Chassis 1 to Chassis 4 are characterized by the presence of four different composite panels layouts as structural elements.

The mass reduction assessment demonstrated that in the Chassis 3 and Chassis 4 the adopted composite panels layouts as a replacement of some previously existing steel tubulars provided a consistent mass reduction around 9% as compared to Chassis 0, along with an extension of the driving range close to 12%. Simultaneously, Chassis 4 provided an increase in the torsional stiffness around 8%. The composite panels layout of the Chassis 4 proved to be an effective way to increase the torsion stiffness of the chassis reducing the structure's weight rather than increase it.

The crash test analyses assessed that all the adopted composite panels layouts are able to stiff the chassis at least as the starting steel tubular layout ensuring a slight increase in the length of the chassis after the impact to protect the passengers and, simultaneously, performing a remarkable reducing of the total mass of the structure, as previously demonstrated. Moreover, the composite panels added in the layouts of Chassis 3 and Chassis 4 demonstrated to be a way to absorb part of the impact energy. Indeed, in Chassis 3, intralaminar damages in the forward corner composite panels were able to absorb an amount of energy around 0.35 kJ, while in Chassis 4 the widespread intralaminar damages of the forward composite panels were able to absorb an amount of energy around 1.3 kJ.

As compared to Chassis 0, in the Chassis 4 the adoption of the composite panels and the damages that occur during the impact provide a gain in the ratio of absorbed energy by more than 7%.

The carried out numerical analyses have preliminarily demonstrated the effectiveness of using composite laminate panels as load-bearing structural elements able to increase the torsional stiffness of a minibus chassis reducing its global mass, to stiffen the chassis to protect passengers and to absorb an amount of impact energy through intralaminar damages.

Funding

Open access funding provided by Università degli Studi della Campania Luigi Vanvitelli within the CRUI-CARE Agreement.

References

1. L. Setlak, R. Kowalik, and T. Lusiak, Practical Use of Composite Materials Used in Military Aircraft, *Materials*, 2021, **14**(17), p 4812.
2. M. Das, S. Sahu, and D.R. Parhi, Composite Materials and Their Damage Detection Using AI Techniques for Aerospace Application: A Brief Review, *Mater. Today: Proceed.*, 2021, **44**, p 955–960.
3. A. Shah Rutvik, et al., "Design and Analysis of Helicopter Tail Using Composite Materials", Recent Advances in Mechanical Engineering. Springer, Singapore, 2023. 703–712
4. M. Eugeni et al., An Industry 4.0 Approach to Large Scale Production of Satellite Constellations. The Case Study of Composite Sandwich Panel Manufacturing, *Acta Astronaut.*, 2022, **192**, p 276–290.
5. B. Stojanović and L. Ivanović, Application of Aluminium Hybrid Composites in Automotive Industry, *Tehnički vjesnik*, 2015, **22**(1), p 247–251.
6. J. Spasenović and I. Blagojević, Composite Materials in Automotive Industry: A Review, *Industrija*, 2021, **49**(2), p 57–68.
7. G.D. Caserta, L. Iannucci, and U. Galvanetto, Shock Absorption Performance of a Motorbike Helmet with Honeycomb Reinforced Liner, *Compos. Struct.*, 2011, **93**(11), p 2748–2759.
8. S.F.K. Sherwani, S.M. Sapuan, Z. Leman, E.S. Zainuddin, and R.A. Ilyas, "Application of polymer composite materials in motorcycles: A Comprehensive review", Biocompos. Synth. Compos. Automot. Appl. (2021): 401–426
9. C. Soutis, Fibre Reinforced Composites in Aircraft Construction, *Prog. Aerosp. Sci.*, 2005, **41**, p 143–151.
10. G. Marsh, "Airbus A350 XWB update", Reinforced Plastics, 2010

11. F. Czerwinski, Current Trends in Automotive Lightweighting Strategies and Materials, *Materials*, 2021, **14**(21), p 6631.
12. N. Fantuzzi, M. Bacciocchi, D. Benedetti, and J. Agnelli, The Use of Sustainable Composites for the Manufacturing of Electric Cars, *Compos. Part C: Open Access*, 2021, **4**, 100096
13. C. Fragassa, A. Pavlovic, and G. Minak, On the Structural Behaviour of a CFRP Safety Cage in a Solar Powered Electric Vehicle, *Compos. Struct.*, 2020, **252**, 112698
14. Q. Liu, Y. Lin, Z. Zong, G. Sun, and Q. Li, Lightweight Design of Carbon Twill Weave Fabric Composite Body Structure for Electric Vehicle, *Compos. Struct.*, 2013, **97**, p 231–238.
15. J.T.J. Burd, E.A. Moore, H. Ezzat, R. Kirchain, and R. Roth, Improvements in Electric Vehicle Battery Technology Influence Vehicle Lightweighting and Material Substitution Decisions, *Appl. Energy*, 2021, **283**, 116269
16. M.A. Caminero, I. Garcia-Moreno, and G.P. Rodriguez, Experimental Study of the Influence of Thickness and Ply-Stacking Sequence on the Compression After Impact Strength of Carbon Fibre Reinforced Epoxy Laminates, *Polym. Test.*, 2018, **66**, p 360–370.
17. G.R. Johnson and W.H. Cook, Fracture Characteristics of Three Metals Subjected to Various Strains, Strain Rates, Temperatures and Pressures, *Eng. Fract. Mech.*, 1985, **21**(1), p 31–48.
18. Abaqus analysis user's manual, version 6.10; 2010
19. X. Wang and J. Shi, Validation of Johnson-Cook Plasticity and Damage Model Using Impact Experiment, *Int. J. Impact Eng.*, 2013, **60**, p 67–75.
20. I. Lapczyk and J. Hurtado, Progressive Damage Modelling in Fibre-Reinforced Material, *Composit.: Part A*, 2007, **38**, p 2333–2341.
21. A. Duarte, A. Díaz Sáez, and N. Silvestre, Comparative Study Between XFEM and Hashin Damage Criterion Applied to Failure of Composites, *Thin-Walled Struct.*, 2017, **115**, p 277–288.
22. V. Acanfora, F. Baldieri, A. Garofano, F. Fittipaldi, and A. Riccio, On the Crashworthiness Behaviour of Innovative Sandwich Shock Absorbers, *Polymers*, 2022, **14**(19), p 4163.
23. V. Acanfora, M. Zarrelli, and A. Riccio, Experimental and Numerical Assessment of the Impact Behaviour of a Composite Sandwich Panel with a Polymeric Honeycomb Core, *Int. J. Impact Eng.*, 2023, **171**, p 0734-743X.